Chinese Chemical Letters 37 (2026) 111693

Contents lists available at ScienceDirect

Chinese Chemical Letters

journal homepage: www.elsevier.com/locate/cclet

Engineering asymmetric electronic structures in Fe-N-S-C nanozymes for dual enzyme-catalyzed-induced ferroptosis and enhanced antitumor efficacy

Jingyao Yu[a,1], Zhuoran Yang[a,b,1], Jian Jiang[c], Mengshu Xu[a], Chunyu Yang[a,*], Zhuo Li[b,*], Wei Guo[a,*]

[a] Key Laboratory of Photochemical Biomaterials and Energy Storage Materials, College of Chemistry and Chemical Engineering, Harbin Normal University, Harbin 150025, China
[b] Key Laboratory of Functional Inorganic Materials Chemistry (Ministry of Education), School of Chemistry and Materials Science, International Joint Research Center for Catalytic Technology, Heilongjiang University, Harbin 150080, China
[c] Department of Ultrasound, Qunli Branch of The First Affiliated Hospital of Harbin Medical University, Harbin 150001, China

ARTICLE INFO

Article history:
Received 24 May 2025
Revised 6 August 2025
Accepted 8 August 2025
Available online 9 August 2025

Keywords:
Ferroptosis
Single-atom nanozymes
Lipid peroxidation
Density functional theory
Tumor therapy

ABSTRACT

Nanozymes, particularly single-atom nanozymes (SAzymes), have gained attention as potential ferroptosis inducers for cancer therapy due to their high catalytic efficiency and selectivity. However, the catalytic activity of SAzymes is often limited by the symmetrical electronic structure at their active sites. To enhance their performance, heteroatom doping strategies have been applied to modulate the electronic properties of SAzyme catalysts. In this study, we synthesized sulfur-doped FNS SAzymes with an Fe-N-S-C asymmetric coordination structure through pyrolysis. Enzyme kinetics analysis and density functional theory calculations revealed that FNS SAzymes exhibit highly efficient peroxidase-like and glutathione oxidase-like activities. These nanozymes are capable of catalyzing the decomposition of H_2O_2 to produce reactive oxygen species and depleting glutathione (GSH), thereby inducing ferroptosis. The FNS SAzymes were combined with an alkyl radical (•R) initiator, 2,2-azobis[2-(2-imidazolin-2-yl)propane] dihydrochloride (AIPH), and assembled into microneedle patches for enhanced ferroptosis therapy (FNSA-MN). Beyond the dual enzyme activities of FNS SAzymes, 808 nm laser activation induced a photothermal effect that facilitated the rapid dissociation of AIPH to generate •R. This FNSA-MN significantly enhanced lipid peroxidation within cells, thereby promoting ferroptosis. *In vivo* studies demonstrated significant suppression of tumor growth and strong anti-metastatic effects, highlighting a promising strategy for localized cancer therapy.

© 2025 Published by Elsevier B.V. on behalf of Chinese Chemical Society and Institute of Materia Medica, Chinese Academy of Medical Sciences.

Ferroptosis represents a newly unveiled type of programmed cell death that relies on iron, whose molecular mechanism primarily relies on the catalytic action of intracellular iron ions to induce lipid peroxidation (LPO) [1,2]. It may result in the disturbance of the lipid bilayer architecture within cell membranes, modifications in membrane permeability, and loss of cellular function [3]. Recent studies have shown that ferroptosis is mainly influenced by the balance of iron, redox status, and lipid metabolism in mammalian cells, and plays a critical role in various pathophysiological processes [4–7]. Contrary to apoptosis and necrosis, ferroptosis is characterized by the disturbance of LPO regulation and the breakdown of antioxidant protective mechanisms, particularly those associated with glutathione (GSH) and glutathione peroxidase 4 (GPX4) [8–11]. Since the identification of Fe_3O_4 nanoparticles (NPs) displaying peroxidase (POD)-mimicking activity, nanomaterials possessing enzyme-like catalytic characteristics have garnered considerable interest owing to their outstanding biocompatibility and stability [12–14]. As research advances, the application of nanozymes in ferroptosis-based cancer therapy has become a promising area of focus. Current ferroptosis inducers include iron alloys [15], iron oxides [16], iron complexes [17], and metal-organic frameworks (MOFs) [18]. These NPs can react in the tumor-specific acidic environment to generate reactive oxygen species (ROS), causing the accumulation of LPO, ultimately leading to tumor cell death [19]. Nevertheless, the catalytic efficacy of the majority of nanozymes is constrained by the fact that merely a limited portion of active sites are present on their surfaces, resulting in low atomic utiliza-

* Corresponding authors.
E-mail addresses: ycy@hrbnu.edu.cn (C. Yang), lizhuo9410@hlju.edu.cn (Z. Li), guowei@hrbnu.edu.cn (W. Guo).
[1] These authors contributed equally to this work.

https://doi.org/10.1016/j.cclet.2025.111693
1001-8417/© 2025 Published by Elsevier B.V. on behalf of Chinese Chemical Society and Institute of Materia Medica, Chinese Academy of Medical Sciences.

tion efficiency, which significantly restricts their overall catalytic effectiveness [20].

In recent years, single-atom nanozymes (SAzymes), known for achieving the highest level of atomic utilization efficiency, have garnered significant attention due to their outstanding catalytic activity and diversity [21–24]. The atomically dispersed structure not only maximizes the utilization of metal (M) atoms but also endows SAzymes with high catalytic activity and selectivity, as the stable M-N_4 coordination sites resemble the structure of metal porphyrins [25–27]. A key challenge in developing highly efficient SAzymes is optimizing the coordination environment of active sites to enhance their enzyme-mimetic activity and elucidate their structure-activity relationship [28]. Despite the exceptional enzyme-mimetic properties exhibited by SAzymes with M-N_4 catalytic sites, their POD-like activity is often suboptimal due to the symmetrical electronic density distribution at the active site [29]. To address this constraint, researchers have put forward the idea of disrupting the symmetrical electronic arrangement of SAzymes in order to regulate the adsorption characteristics of reaction intermediates at the active site [30]. The heteroatom doping strategy (X = O, P, S) effectively tunes the electronic structure of the M-N_4 active center, thereby enhancing its catalytic activity [31–33]. The N atoms directly bonded to the central metal atom constitute the first coordination shell [34]. For instance, Niu *et al.* developed a Cu-N_3S SAzymes (Cu-NS@UK@PO_x) co-loaded with UK5099 and pyruvate oxidase (PO_x). By substituting the nitrogen in the first coordination layer with weakly electronegative sulfur (S), they altered the original spatial symmetry of the Cu-N-C electronic distribution, effectively modulating the enzyme-mimetic catalytic process [35]. When heteroatoms are doped into the second coordination shell of M-N_4, they can modify the electronic density of the metal center, thereby influencing its ability to adsorb and activate reactants. Recent studies have demonstrated that Fe-N-C catalysts doped with S atoms in the second coordination shell exhibit superior performance in the oxygen reduction reaction (ORR) compared to their phosphorus-doped counterparts [36]. This enhancement is primarily attributed to the electronic properties of S. Unlike phosphorus, which has higher electronegativity and weaker electron-donating capability, sulfur can more effectively modulate the d-orbital energy levels of the Fe center. This adjustment improves the adsorption and activation of O_2 molecules on the catalyst surface. Moreover, due to the relatively small atomic radius of sulfur, its incorporation into the second coordination shell does not impose significant steric hindrance around the Fe-N-C active site. Drawing inspiration from this, it is anticipated that the precise regulation of electron cloud distribution through heteroatom doping will further augment the catalytic activity and therapeutic efficacy of SAzymes in tumor therapy. This strategy provides a novel approach for designing highly efficient and stable SAzymes.

Microneedle (MN) technology is an advanced transdermal drug delivery method that utilizes MN arrays to painlessly penetrate the stratum corneum (SC) and facilitate drug transport with minimal invasiveness [37,38]. Given that breast cancer is a superficial tumor, the application of MN-based transdermal drug delivery offers substantial advantages [39]. MNs can bypass the SC barrier and directly deliver therapeutic agents to the target site, thereby avoiding hepatic first-pass metabolism and gastrointestinal degradation, significantly improving the bioavailability of the drug [40]. Furthermore, this administration route minimizes systemic toxicity and reduces adverse systemic side effects, offering a safe and efficient localized drug delivery strategy for breast cancer treatment [41].

In this study, we developed an integrated MN patch (FNSA-MN) combining Fe-N-S-C coordination structure SAzymes (FNS SAzymes) and the alkyl radical initiator 2,2-azobis[2-(2-imidazolin-2-yl)propane] dihydrochloride (AIPH) for improved ferroptosis therapy (Fig. S1 in Supporting information). Zeolitic imidazolate framework-8 (ZIF-8) was synthesized using a liquid-phase method, with iron sources and dopants uniformly dispersed in the precursor. Pyrolysis produced Fe-N-S-C coordination structure SAzymes. Enzyme kinetics revealed that sulfur doping enhanced the POD-like and glutathione oxidase (GSHOx)-like activities of FNS SAzymes. Density functional theory (DFT) calculations showed that sulfur doping shifted the electronic cloud at the interface, improving catalytic efficiency and boosting dual-enzyme activity. FNS SAzymes and AIPH were loaded onto MN tips. When MNs degraded at the tumor site in mice, they catalyzed the breakdown of H_2O_2, generating toxic hydroxyl radicals (•OH) and promoting LPO. Additionally, FNS SAzymes depleted intracellular GSH, increasing oxidative stress in tumor cells. Under 808 nm laser stimulation, FNS SAzymes exhibited thermal effects, while AIPH generated •R upon heat dissociation, further increasing LPO and enhancing ferroptosis. FNSA-MN also activated the immune system in 4T1 tumor-bearing mice, showing promising anti-lung metastatic potential.

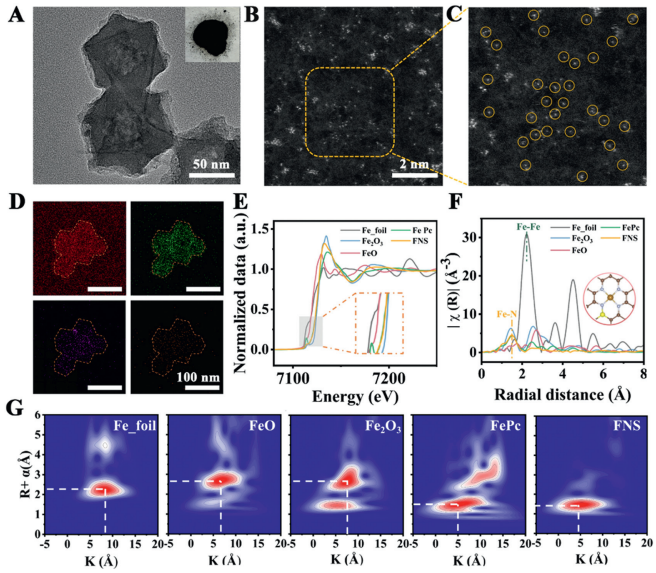


Fig. 1. (A) TEM image of FNS SAzymes. (B) HAADF-STEM image, and (C) an enlarged view of FNS SAzymes. (D) EDS mapping images of FNS SAzymes. (E) Normalized Fe K-edge XANES spectra, (F) FT-EXAFS spectra at R-space, and (G) Wavelet transform EXAFS of FNS SAzymes with Fe_2O_3, FeO and Fe foil as the references.

The fabrication procedures of FNS SAzyme are illustrated in Fig. S2 (Supporting information). Initially, we successfully synthesized ZIF-8 using the classic liquid-phase direct synthesis method at room temperature, resulting in a white powder. As shown in Fig. S3 (Supporting information), the scanning electron microscope (SEM) and transmission electron microscopy (TEM) images further characterized ZIF-8, demonstrating a well-defined, regular dodecahedral structure (Figs. S3A and D). To improve the performance of ZIF-8, we introduced Fe and S elements, which caused the powder to change color from white to yellow to obtain the FNS SAzymes precursor. Interestingly, while the introduction of Fe and S did not significantly alter the skeletal features of ZIF-8, it did make the NP surfaces noticeably rougher (Figs. S3B and E). The FNS SAzymes precursor was then subjected to pyrolysis at 700 °C for 2 h under an argon atmosphere, resulting in the formation of a black powder. FNS SAzymes largely retained their initial dodecahedral morphology, exhibited a relatively uniform particle size distribution, and displayed a well-defined layered porous structure (Fig. 1A, Figs. S3C and S4 in Supporting information). To evaluate the pH-responsive stability of FNS SAzymes, we mea-

sured their hydrodynamic sizes in buffer solutions of varying pH values. As shown in Fig. S5 (Supporting information), the hydrodynamic diameters of FNS SAzymes exhibited negligible changes across different pH conditions, indicating the absence of significant aggregation. These results collectively demonstrate the excellent stability of FNS SAzymes under diverse pH environments and physiological environment. To investigate the specific surface area and pore size distribution of FNS SAzymes, nitrogen adsorption-desorption isotherms were measured (Fig. S6 in Supporting information). The isotherm exhibited the characteristics of a type IV isotherm with an H4-hysteresis loop, confirming that FNS SAzymes are a mesoporous material. Energy dispersive spectrometer (EDS) images further confirmed the uniform distribution of C, N, Fe, and S in FNS SAzymes (Fig. 1D), indicating successful Fe loading with high dispersion. X-ray diffraction (XRD) analysis revealed characteristic diffraction peaks of carbon at 25° and 44° (Fig. S7 in Supporting information), corresponding to the (002) and (101) planes of carbon, respectively. No diffraction peaks related to metallic Fe were observed, suggesting that Fe in FNS SAzymes may exist in an amorphous or highly dispersed form. High-resolution transmission electron microscopy (HRTEM) observations revealed no lattice fringes corresponding to elemental iron in FNS SAzymes (Fig. S3F). Additionally, high-angle annular dark-field scanning transmission electron microscopy (HAADF-STEM) images revealed numerous highly dispersed white spots (marked by yellow circles), indicating the presence of isolated single Fe atoms on FNS SAzymes (Figs. 1B and C).

X-ray photoelectron spectroscopy (XPS) was further employed to analyze the chemical environment and elemental states in the FNS SAzymes. In the C 1s spectrum, the prominent peak at 284.8 eV corresponds to C-C or C=C bonds; the peak at 285.9 eV is attributed to C-N or C-S bonds, and the peaks at 287.0 and 288.7 eV correspond to C=O and O-C=O bonds, respectively. As shown in Fig. S8 (Supporting information), this result indicates that the carbon atoms in the material possess multiple distinct chemical environments (Fig. S8A) [42]. In the N 1s spectrum, FNS SAzymes shows characteristic peaks at 398.8, 401.2, and 402.4 eV, corresponding to pyridine nitrogen, pyrrole nitrogen, and graphite nitrogen, respectively (Fig. S8B) [43]. Additionally, an absorption peak at 399.8 eV was observed, indicating the presence of an Fe-N coordination structure in the sample (Fig. S8E). Furthermore, the Fe 2p XPS spectrum of FNS SAzymes shows characteristic signals of Fe $2p_{3/2}$ and Fe $2p_{1/2}$ at 711.2 and 725.2 eV, respectively, which are higher than the Fe^0 peak at 707.0 eV, confirming that all forms of Fe exist in an oxidized state (Fig. S8C) [44]. Notably, in comparison to FN SAzymes, the Fe peak in FNS SAzymes undergoes a shift toward lower binding energy, while the N peak shifts to a higher binding energy (Fig. S8F). This supports the successful introduction of S into the structure, which in turn affects the charge distribution. Fig. S8D illustrates that the two prominent peaks, located at 163.1 and 164.8 eV, are respectively associated with the $2p_{3/2}$ and $2p_{1/2}$ peaks characteristic of C-S-N within the S 2p XPS spectrum [45]. Importantly, the XPS analysis indicates that there are no Fe-S bonds in FNS SAzymes, ruling out the possibility of direct Fe-S coordination. Both FN SAzyme and FNS SAzyme exhibited a characteristic Fe-N stretching vibration at 593 cm^{-1}, while no detectable Fe-S vibrational signature was observed in the FNS SAzyme spectrum. This further confirms the successful formation of Fe-N coordination without the incorporation of Fe-S bonds. Combined with XPS and synchrotron-based characterizations, the coordination mode of sulfur in the FNS SAzyme was further identified as Fe-N-S-C (Fig. S9 in Supporting information). The Fe K-edge X-ray absorption near edge structure (XANES) and extended X-ray absorption fine structure (EXAFS) analyses provide precise confirmation of the electronic state and coordination environment of Fe species in FNS SAzymes. As shown in Fig. 1E, XANES spectra were collected at the Fe K-edge for FNS and several reference materials (Fe-foil, FeO, Fe_2O_3, and FePc). Notably, the absorption edge of FNS SAzymes lies between those of FeO and Fe_2O_3, indicating the presence of $Fe^{\delta+}$ ($2 < \delta < 3$) in the material, corresponding to an oxidation state between Fe^{2+} and Fe^{3+}. This finding is consistent with the XPS analysis. The Fourier-transform EXAFS (FT-EXAFS) of Fe K-edge extended spectrum further reveals the local coordination environment of Fe atoms in FNS (Fig. 1F). The fitting results show that the peak position of Fe species in FNS is closer to that of the FePc reference, with a peak at approximately 1.4 Å (uncorrected phase shift), which is attributed to the characteristic Fe-N bond. Simultaneously, no peak at 2.1 Å is observed, which clearly corresponds to the Fe-Fe peak in the Fe foil. This suggests that the FNS does not contain metallic Fe NPs, highlighting the single-atom dispersion of Fe in FNS SAzymes. In agreement with the Fourier transform results, the wavelet transform contour plots display a prominent peak at approximately 5.01 Å in k-space, resembling the peak observed in FePc and clearly differing from other reference signals (Fig. 1G).

FNS SAzymes NPs exhibit superior light absorption properties in the 200–2500 nm wavelength range compared to ZIF-8 and the precursor of FNS SAzymes, with particularly enhanced absorption in the NIR region (Fig. S10 in Supporting information). As shown in Fig. S11 (Supporting information), experimental data revealed a significant increase in temperature with the rising concentration of the material and laser power density (Figs. S11A and B). Further photothermal stability tests demonstrated that, after three on/off cycles, the photothermal performance of FNS SAzymes remained stable, showing no noticeable changes, thus confirming their excellent photothermal stability (Fig. S11C). Additionally, the photothermal conversion efficiency of FNS SAzymes was calculated to be 23.9% (Fig. S11D), indicating that FNS SAzymes serve as highly effective photothermal agents. Previous studies have indicated that endogenous H_2O_2 within tumor cells can be catalytically converted into $^{\bullet}OH$ by nanoenzymes, offering a promising approach for tumor catalytic therapy [46]. To assess the POD-like activity of FNS SAzymes, a reference enzyme without S coordination was synthesized by preparing FN SAzymes, which lack the sulfur coordination typical of FNS SAzymes. As shown in Fig. S12 (Supporting information), compared to FN, FNS is capable of inducing a more extensive chemical reaction in H_2O_2, generating higher amounts of $^{\bullet}OH$, which subsequently catalyze the oxidation of TMB to form a blue oxidized TMB (oxTMB) detectable at 655 nm. This confirms that FNS SAzymes exhibit POD-like activity (Fig. 2A and Fig. S12A). As shown in Fig. S12B, FNS SAzymes exhibit pH-dependent activity, with a 1.5-fold increase in acidic buffer (pH 5.4) compared to neutral buffer (pH 7.4), indicating stronger POD-like activity under acidic conditions.

Additionally, the generation of $^{\bullet}OH$ increases with FNS SAzymes concentration, showing a clear concentration-dependent trend, suggesting effective promotion of H_2O_2 decomposition to generate $^{\bullet}OH$ (Fig. S12C). To further assess the ability of FNS SAzymes to catalyze H_2O_2 decomposition, ESR spectroscopy was employed, revealing the characteristic 1:2:2:1 multiplet pattern. The results indicated that FNS SAzymes generate more $^{\bullet}OH$ under identical conditions (Fig. 2B). Subsequently, the Michaelis-Menten kinetics of FNS SAzymes was analyzed at pH 5.4, using a fixed concentration of TMB and SAzymes while varying the H_2O_2 concentration from 1 mmol/L to 60 mmol/L. The kinetic parameters for the POD substrate H_2O_2 were obtained. As shown in Figs. 2C and D, the K_m value and maximum reaction rate (V_{max}) for FNS SAzymes were 3.71 mmol/L and 1.896×10^{-7} mol L^{-1} s^{-1}, respectively, while for FN, the K_m and V_{max} values were 14.83 mmol/L and 1.405×10^{-7} mol L^{-1} s^{-1}. The faster reaction rate of FNS SAzymes reflects its stronger POD-like activity compared to FN SAzymes. DFT calculations on Fe-N-C and Fe-N-S-C structures revealed that S doping

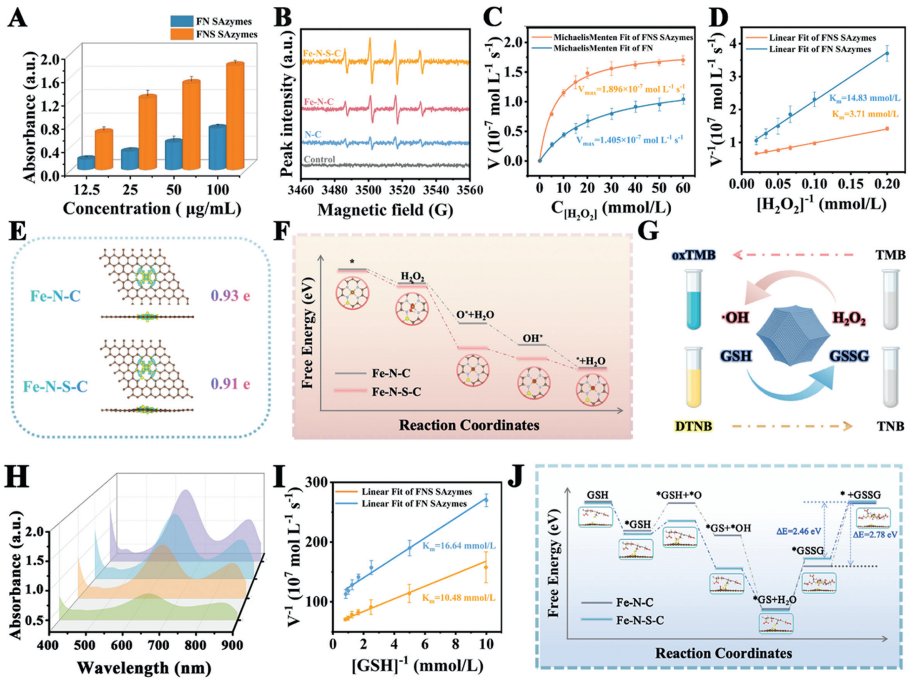


Fig. 2. (A) Utilization of a TMB probe for the identification of ·OH generation across diverse experimental groups within PBS at different concentrations. (B) ESR spectra of various experimental groups detected through the application of a DMPO probe. (C) Michaelis-Menten kinetic analysis and (D) Lineweaver-Burk plots of FN SAzyme and FNS SAzyme for POD-like activity with H_2O_2 as the substrate. (E) The charge density difference and Bader charges of FN SAzyme and FNS SAzyme. (F) Free energy diagrams of POD-like activity for FN SAzyme and FNS SAzyme. (G) The POD-like and GSHOx-like activities of FNS SAzyme. (H) Time-dependent UV/vis absorption changes in GSH depletion detection upon the addition of FNS SAzyme. (I) Lineweaver-Burk plots of FN SAzyme and FNS SAzyme for GSHOx-like activity with GSH as the substrate. (J) Free energy diagrams of GSHOx-like activity for FN SAzyme and FNS SAzyme. All data are presented as the mean ± SD ($n = 3$).

distorts the N atom plane and alters charge distribution due to S's larger atomic radius and lower electronegativity. Bader analysis showed Fe in Fe-N-S-C carries a slightly lower charge (0.91 e) than in Fe-N-C (0.93 e), suggesting reduced electron depletion and enhanced catalytic activity (Fig. 2E). To understand the catalytic mechanism of Fe-N-C and Fe-N-S-C active sites during H_2O_2 activation, we conducted DFT calculations to elucidate the catalytic pathway (Fig. S13 in Supporting information). The results indicate that the adsorption capacity of Fe-N-S-C for H_2O_2 is comparable to that of Fe-N-C (Fig. S14 in Supporting information). This may be attributed to the optimized H_2O_2 molecules more readily attaching to the single Fe atom in the Fe-N-S-C/Fe-N-C configuration, facilitating subsequent decomposition. The adsorbed H_2O_2 undergoes further dissociation, generating an activated O atom and a H_2O molecule ($O^* + H_2O$), leading to the formation of a single adsorbed OH* at the catalytic site. Ultimately, the adsorbed $^*H_2O$ is released and the catalytic site ($^* + H_2O$) is re-exposed. Comparative analysis demonstrates that the Fe site in the Fe-N-S-C configuration exhibits superior catalytic performance, enabling faster and more efficient generation of ·OH, further confirming its excellent enzymatic activity (Fig. 2F).

Although FNS SAzymes exhibit a clear advantage in generating ROS under mildly acidic conditions, the excessive presence of GSH within the tumor microenvironment (TME) can mitigate ROS-induced oxidative stress by neutralizing the generated ROS. Therefore, the presence of GSHOx-like activity in FNS SAzymes is crucial, as it allows for the consumption of GSH by oxidizing it into GSSG (Fig. 2G). To assess this, as shown in Fig. S15 (Supporting information), FNS SAzyme solutions were mixed with GSH solutions, and the GSH content was quantified at different time points using DTNB. The results indicated a significant decrease in absorbance at 412 nm over time, demonstrating that FNS SAzymes possess GSHOx-like activity and effectively deplete GSH (Fig. 2H and Fig. S15A). Moreover, their GSH depletion capability was found to surpass that of the other two groups. It should be emphasized that pH levels exert an influence on catalytic activity, as evidenced by FNS SAzymes exhibiting increased GSH consumption within a simulated, mildly acidic tumor microenvironment (Fig. S15B). During the GSH catalytic reaction, FNS SAzymes exhibited typical Michaelis-Menten kinetics (Fig. 2I and Fig. S16 in Supporting information). The calculated V_{max} and K_m values were 10.48 mmol/L and 1.562×10^{-6} mol L^{-1} s^{-1}, respectively, representing a significant improvement over FN. DFT analysis revealed that in both structural configurations, the S atom in the GSH molecule can interact with the Fe site at the Fe-N-S-C interface, facilitating GSH adsorption. Following this, an O atom from water can bind to the active site, promoting the conversion of GSH. The adsorbed GSH reacts with O, generating *GS and *OH in the adsorbed state. Subsequently, another GSH molecule can react with OH, forming *GS and H_2O. Finally, *GS can undergo coupling to form GSSG (Fig. S17 in Supporting information). As shown in Fig. 2J, the total Gibbs free energy of the Fe site in the Fe-N-S-C configuration was the lowest among these models, indicating its high-efficiency GSHOx-like activity. In summary, the Fe-N-S-C catalytic site significantly enhances the POD-like and GSHOx activity of FNS SAzymes. Our results reveal that FNS-SAzymes also exhibit catalase-like activity, as demonstrated in Fig. S18 (Supporting information). This catalase-mimicking functionality enables FNS-SAzymes to decompose endogenous H_2O_2 and generate oxygen within TEM. The *in situ* oxygen production is particularly beneficial during treatment, as it helps alleviate tumor hypoxia and enhances therapeutic efficacy.

AIPH, as a typical ·R precursor, rapidly dissociates to generate ·R upon binding to the photothermally effective FNS SAzyme under laser irradiation [47]. To evaluate the stability of AIPH, we employed ABTS as a probe to monitor the generation of ·R in phosphate buffered saline (PBS) buffer at 37 °C. This approach allowed us to assess its radical-releasing behavior under physiologically rel-

evant conditions. The results demonstrated that AIPH also maintained good stability under simulated physiological conditions (Fig. S19 in Supporting information). This process significantly amplifies intracellular LPO level, thereby enhancing ferroptosis. MN technology offers a promising platform for more efficient delivery of agents to enhance therapeutic outcomes. In this study, we first attempted to fabricate MNs using sodium alginate (SA) hydrogel. At 20 mg/mL, SA's insufficient fluidity hindered the process. We then investigated SA solutions at various concentrations, finding that a 5 mg/mL solution couldn't form a complete MN structure, while a 10 mg/mL solution exhibited excellent needle formation properties (Fig. S20 in Supporting information), and thus, it was selected as the optimal concentration. Given that SA and polyvinyl alcohol (PVA) can undergo inter-molecular crosslinking through repeated freeze-thaw cycles, we further introduced PVA into the SA system for composite modification. By comparing the morphological characteristics and mechanical strength of MNs at different PVA concentrations (Fig. S21 in Supporting information), we determined that 0.1 g/mL was the optimal concentration for PVA addition. In order to augment the mechanical attributes of the MNs even further, we incorporated polyvinylpyrrolidone (PVP) into the SA-PVA composite system. Our findings indicated that the amount of PVP added had a significant impact on MN performance: excessive PVP concentrations led to increased brittleness and breakage of the MNs (Fig. S22 in Supporting information), while a moderate addition of both PVA and PVP notably improved the mechanical strength of the MNs. This trend was further confirmed in Fig. S23 (Supporting information). In this experiment, MNs were fabricated using a vacuum-assisted centrifugation method. As shown in Fig. S24 (Supporting information), through this method, FNS SAzymes and AIPH were successfully concentrated at the tips of the MNs, referred to as FNSA-MNs (Fig. S24A). The fabricated MN system displayed a regular 10×10 array arrangement, with each needle having a uniform conical structure. SEM characterization revealed that the needle height was approximately 800 μm, with a base diameter of about 300 μm and an inter-needle spacing of 650 μm (Figs. S24B and C). Considering the thickness of the human skin SC is only 15–20 μm, this MN design ensures effective penetration through the SC barrier, enabling precise drug delivery to the targeted skin lesions. To further assess the mechanical performance of the MNs, we conducted a foil penetration test (thickness = 15 μm). The results showed that after multiple punctures, as shown in Fig. S25 (Supporting information), the MNs loaded with FNS SAzymes and AIPH only exhibited minimal tip damage (Fig. S25A). A comparison of the mechanical strength between blank MNs and drug-loaded MNs revealed that drug loading had minimal impact on the structural integrity and mechanical properties of the MNs, though it did cause a noticeable color change. This finding confirms that the drug-loaded system maintains its mechanical performance while effectively delivering the drug (Fig. S25B). To evaluate the photothermal effects of FNSA-MNs *in vitro*, samples were divided into experimental (808 nm laser) and control (no laser) groups. Infrared imaging showed a significant temperature rise in the experimental group. As shown in Fig. S26 (Supporting information), further tests with varying laser power densities (0.5–2 W/cm^2) revealed that at 1 W/cm^2, FNSA-MNs reached temperatures sufficient for effective tumor photothermal therapy (PTT) (Figs. S26A and C). After six laser on/off cycles, FNSA-MNs maintained stable photothermal conversion with no noticeable decline (Fig. S26B), confirming excellent photothermal stability for tumor therapy.

To further investigate the drug release properties of FNSA-MNs, we systematically studied the release behavior of AIPH in buffer solution under both laser-irradiated and non-irradiated conditions. Quantitative analysis based on the standard curve revealed that in the absence of laser irradiation, approximately 70% of AIPH was released from the FNSA-MNs within 45 min. As shown in Fig. S27 (Supporting information), in contrast, under 808 nm laser irradiation, nearly 100% of AIPH was released in the same time period. This significant difference not only confirmed that laser irradiation can significantly enhance the release kinetics of AIPH but also accelerated the decomposition of AIPH, facilitating the generation of $^{\bullet}$R (Figs. S27A and B). As illustrated in Fig. S27C, the release profiles under both laser-irradiated and non-irradiated conditions conformed well to a typical first-order release pattern. Notably, AIPH release was significantly accelerated under laser exposure, with a marked increase observed at 45 min. It is worth noting that under physiological conditions simulating normal tissue (pH 7.4), even in the presence of laser irradiation, the cumulative release of AIPH reached only 61.4%. In contrast, under acidic conditions mimicking TME (pH 5.4), the FNSA-MN microneedle system demonstrated superior controlled-release behavior, leading to a substantially enhanced AIPH release (Fig. S27D). These results highlight the system's pH-responsive and photo-triggered drug release capabilities, making it well-suited for tumor-targeted therapeutic applications. To visually demonstrate the laser-induced dissolution of the MNs, we utilized methylene blue as a marker and conducted an *in vitro* simulation experiment to observe the diffusion behavior of the MNs within a gelatin matrix (mimicking mouse skin). The findings indicated that the MNs within the laser-treated cohort displayed notably enhanced dissolution rates and a more extensive diffusion depth of methylene blue when contrasted with the control group (Figs. S27E and F), further confirming that laser irradiation effectively accelerates the MN dissolution process. This finding provides important experimental support for the application of FNSA-MNs.

Utilizing the strong enzymatic activity of FNS SAzymes, we examined their therapeutic effect on 4T1 tumor cells. MTT assays showed that FNS SAzymes@AIPH reduced 4T1 cell viability to 70% at 200 μg/mL, indicating significant cytotoxicity. As shown in Fig. S28 (Supporting information), AIPH alone without laser had no enhanced effect, confirming its thermal activation dependence (Fig. S28A). Biocompatibility tests on L929 normal cells showed over 90% viability at all concentrations, demonstrating the excellent safety profile of FNS SAzymes (Fig. S28B). As shown in Fig. S28C, FNS caused moderate cytotoxicity to L929 cells under laser due to its strong photothermal effect. Co-treatment with FNS and AIPH enhanced cell killing, indicating a synergistic effect under photoactivation. Although FNS SAzymes may affect normal cells, the use of a MN patch allows localized delivery to tumors, minimizing off-target damage. Additionally, biocompatibility tests of the MN matrix materials (SA, PVA, PVP) on L929 and 4T1 cells (Fig. S28D) showed over 95% viability, confirming their safety for normal cells. In order to explore the enzymatic activity of FNS SAzymes and the role of $^{\bullet}$R in inducing ferroptosis in tumor cells, we conducted further experiments by dividing the cells into five groups: (i) control, (ii) laser, (iii) FNS, (iv) FNS+laser, (v) FNS+AIPH+laser. First, we assessed the depletion of intracellular GSH levels. FNS demonstrated superior GSH oxidase-like activity, with the FNS+AIPH+laser group exhibiting the highest level of GSH consumption, indicating that under the influence of photothermal and $^{\bullet}$R, this treatment holds considerable potential for inducing ferroptosis (Fig. S29 in Supporting information). Intracellular ROS levels, measured using DCFH-DA (Fig. S30A in Supporting information), revealed weak fluorescence in the laser group, while FNS treatment induced stronger ROS signals. As shown in Fig. 3, the combination of laser and AIPH further elevated ROS levels, likely due to higher temperature and enhanced LPO reactions (Fig. 3C and Fig. S30B in Supporting information). In the DAPGreen probe images depicting autophagy, we observed the most prominent autophagic activity in cells treated with FNS+AIPH+laser (Fig. S31 in Supporting information).

The accelerated fusion of autophagosomes and lysosomes leads to extensive degradation of intracellular materials, resulting in the release of iron and intensification of ferroptosis. LPO accumulation

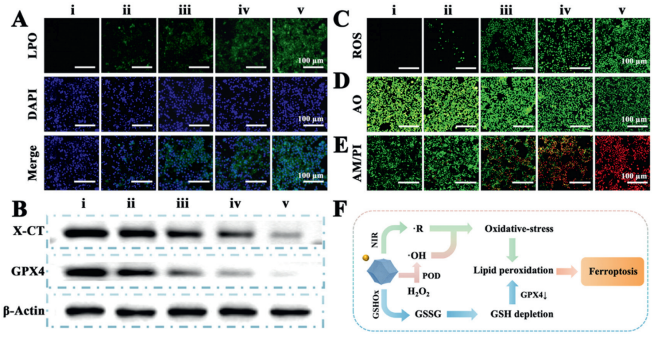


Fig. 3. (A) Fluorescence microscopy to observe the intracellular distribution of BODIPY 581/591-C11-indicated peroxides in 4T1 and (B) Western blot analysis of 4T1 cell extracts cells after different treatments. (C) The fluorescence microscopy images of intracellular ROS production in different treatment groups using DCFH-DA probe. (D) Assessment of lysosomal membrane integrity in 4T1 cells after different treatments using AO probes. (E) The fluorescence microscopy images of 4T1 cells stained with calcein-AM/PI after different treatments (scale bar: 100 μm). (F) Schematic mechanism of FNSA-MNs enabled 4T1 cell ferroptosis.

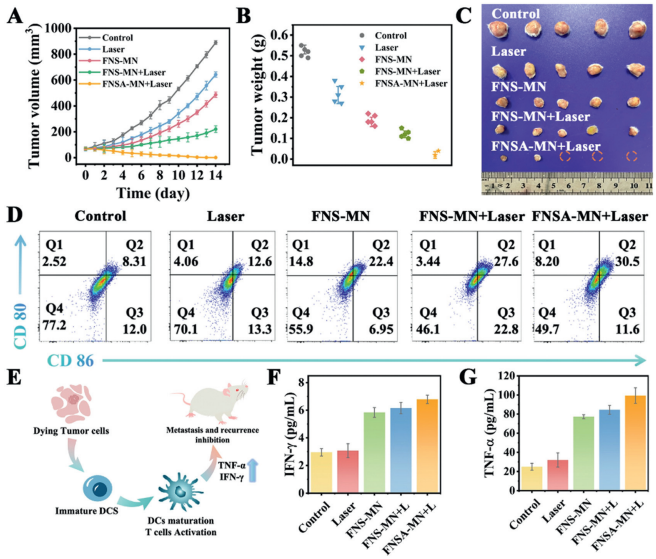


Fig. 4. (A) Relative tumor volumes after different treatments of mice. (B) Changes in the average tumor weight for the different groups after the 14 days of treatment. (C) Representative images of tumors in mice after 14 days of treatment. (D) The flow cytometry analysis of CD80 and CD86 expression after different treatments for 4T1 tumor-bearing mice. (E) Schematic illustration of FNSA-MN+laser for potentiating immunotherapy. Cytokines level of (F) IFN-γ and (G) TNF-α in plasma collected by using ELISA. Data are presented as mean ± standard deviation (SD) ($n = 5$).

is a key feature of ferroptosis. Using the C11-BODIPY581/591 probe, strong green fluorescence was observed in FNS-treated 4T1 cells (Fig. 3A and Fig. S31), indicating ROS-induced LPO buildup. The FNS+AIPH+laser group showed the highest fluorescence, linked to increased ·OH levels from enzyme catalysis and photothermal-enhanced ·R. X-CT is involved in the uptake of oxidized cysteine (the oxidized form of cysteine) from the extracellular space into the cytoplasm [48]. Blocking X-CT activity impairs GSH synthesis, lowers intracellular GSH levels, and consequently reduces both the activity and expression of GPX4. Given that GSH acts as a cofactor in GPX4-mediated lipid repair, FNS-induced GSH depletion likely leads to downregulation of GPX4 [49]. Western blot analysis revealed a significant reduction in X-CT and GPX4 expression in 4T1 cells after FNS treatment, confirming the occurrence of ferroptosis (Fig. 3B and Fig. S32 in Supporting information). The FNS+AIPH+laser group exhibited the most pronounced reduction in X-CT and GPX4 expression, suggesting the highest degree of ferroptosis. Next, we performed AO staining to assess the integrity of lysosomal membranes in 4T1 cells. Following AO staining, healthy cells showed yellow-green fluorescence, whereas apoptotic cells displayed green fluorescence. Among the multitude of groups examined, the FNS+AIPH+laser group exhibited the most pronounced green fluorescence (Fig. 3D), indicative of substantial lysosomal membrane disruption.

To evaluate mitochondrial impairment in 4T1 cells, we utilized the JC-1 probe to monitor alterations in mitochondrial membrane potential across the diverse groups. Notably, the control and laser groups displayed negligible green fluorescence (Fig. S33 in Supporting information), while the FNS+AIPH+laser group displayed notable mitochondrial damage. This indicates that the multi-pathway induction of ferroptosis *via* enzyme catalysis and PTT significantly exacerbates mitochondrial damage, thereby enhancing the cytotoxic effect on tumor cells. As shown in Fig. 3E and Fig. S34 (Supporting information), we utilized the calcein-AM and PI double-staining method to assess the therapeutic efficacy of different treatment groups on 4T1 cells. The results revealed that the FNS+AIPH+laser group showing the most intense red fluorescence. This indicates that the FNS+AIPH+laser treatment not only generates substantial ROS to kill tumor cells through the material's inherent properties but also synergizes with photothermal-triggered AIPH to produce ·R, leading to a significantly enhanced antitumor effect. The above results indicate that the use of FNSA-MNs significantly enhances the induction of ferroptosis in tumor cells *in vitro* (Fig. 3F).

Encouraged by the promising *in vitro* results and the enhanced antitumor effects that promotes ferroptosis in tumor cells by increasing LPO levels, we proceeded with a preliminary *in vivo* investigation on 4T1 tumor-bearing mice. All animal experiments were reviewed and approved by the Ethics Research Committee of Harbin Normal University (No. HNUARIA2022003). As shown in Fig. S35 (Supporting information), the treatment protocol is outlined (Fig. S35A). When the tumor size reached ~50 mm^3, the tumor-bearing mice were randomly assigned into five treatment groups: (i) control, (ii) laser group, (iii) FNS-MN group, (iv) FNS-MN+laser group, and (v) FNSA-MN+laser group. The fabricated MNs were carefully inserted into the tumor site of the mice. After 2 min of precise localization, they were easily removed, with the puncture channels observed to gradually close over time, achieving self-healing within 10 min (Fig. S35B). This confirmed the excellent minimally invasive nature of the system. Under near-infrared laser irradiation (808 nm, 1 W/cm^2), it was found that the tumor temperature in the laser-only group increased minimally (ΔT < 2 °C), while the FNS-MN+laser and FNSA-MN+laser groups exhibited significant photothermal conversion ability. The local tumor temperature in these groups reached approximately 60.0 °C (Figs. S35C and D). Tumor volume monitoring demonstrated that, compared to the control group, the FNS-MN group exhibited moderate tumor suppression, primarily attributed to ferroptosis induced by the dual-enzyme activity (Fig. 4A and Fig. S36 in Supporting information). However, the FNS-MN+laser group showed enhanced tumor inhibition, as the photothermal effect further activated POD-like and GSHOx-like, amplifying ferroptosis. The FNSA-MN+laser group displayed the most pronounced tumor suppression, primarily due to the additional heat promoting the release of ·R. The combined dual-enzyme activity of FNSA-MN further enhanced ferroptosis, leading to optimal antitumor effects. After 14 days, the relative tumor weight and images are shown Figs. 4B and C, with tumor weight differences among the treatment groups consistent with the tumor growth curves. It is noteworthy that no significant weight loss was observed in the FNSA-MN+laser group mice during the treatment period (Fig. S37 in Supporting information).

To assess clearance and biosafety of the FNSA-MN system, inductively coupled plasma-mass spectrometry (ICP-MS) was used to monitor urinary iron levels after FNSA-MN+laser treatment. Iron levels gradually declined over 14 days, indicating renal excretion. Biodistribution analysis showed iron mainly accumulated in the liver, suggesting hepatic metabolism (Fig. S38 in Supporting information). Furthermore, Hematological analysis across treatment groups showed no significant changes in white blood cells (WBC), red blood cells (RBC), platelets (PLT), mean corpuscular hemoglobin (MCH), mean corpuscular volume (MCV), hematocrit (HCT), hemoglobin concentration (HGB), and mean corpuscular hemoglobin concentration (MCHC), confirming good systemic biocompatibility of the FNSA-MN therapy (Fig. S39 in Supporting information). No significant damage was observed in these organs (heart, liver, spleen, lungs, and kidneys), indicating the safety of the combined FNSA-MN+laser treatment. Hematoxylin-eosin (H&E) staining of 4T1 tumor tissue sections revealed typical nuclear dissolution in the treatment groups, indicating severe tumor cell damage (Fig. S40 in Supporting information). These findings demonstrate that the enhanced enzymatic activity of FNSA-MN and the release of $^{\bullet}R$ significantly potentiated ferroptosis, effectively inducing tumor cell death *in vivo*. Dendritic cells (DCs) are crucial antigen-presenting cells in innate and adaptive immunity. Upon antigen exposure, immature DCs mature and spread, especially in the lymphatic system and spleen [50–52]. This study evaluated how various treatments affect DC maturation. We measured CD80 and CD86, key maturation markers, by flow cytometry to assess DC maturation (Fig. 4D) [53–55]. Compared to the control group (8.3%) and the laser group (12.6%), the FNS-MN group (22.4%), FNS-MN+laser group (27.6%), and FNSA-MN+laser group (30.5%) exhibited significantly higher maturation rates of DCs, suggesting that these treatments effectively enhanced the tumor immunogenic response. Mature DCs present antigen peptides to naïve T-cells *via* major histocompatibility complex (MHC) molecules and secrete cytokines to regulate T-cell activation, proliferation, and differentiation. To assess the immune modulation induced by these treatments, we collected serum samples from the blood of mouse ocular veins in each group and analyzed immune-regulatory cytokines, including tumor necrosis factor (TNF-α) and interferon-gamma (IFN-γ), using enzyme-linked immunosorbent assay (ELISA) (Fig. 4E). The FNSA-MN+laser group showed the highest expression levels of these cytokines, confirming that the combination therapy effectively stimulates the immune system (Figs. 4F and G).

To systematically evaluate the inhibition of tumor lung metastasis by the FNSA-MN-mediated ferroptosis-enhanced therapy, we established a 4T1 tumor-bearing mouse model. Both the FNSA-MN+laser and untreated groups were injected with 4T1 tumor cells *via* the tail vein on day 8. As shown in Fig. S41 (Supporting information), all mice were sacrificed on day 30, and lung tissues were collected for metastatic nodule counting, with metastatic foci highlighted by red circles (Figs. S41A and B). Remarkably, the FNSA-MN+laser group exhibited an absence of discernible metastatic nodules, a stark disparity from the multitude of nodules observed in the control group. These observations were further substantiated by histological assessment of lung tissue *via* H&E staining (Fig. S41C). During the experiment, the physiological status of the mice was monitored, revealing that the treatment group maintained stable body weight with a slight upward trend, whereas the control group showed significant weight loss and worsening physiological conditions after 8 days of tumor cell inoculation (Fig. S41D). These results suggest that the combination of FNSA-MN and laser irradiation can significantly inhibit primary tumor growth and effectively block tumor metastasis through a synergistic enhancement of ferroptosis.

In summary, we synthesized FNS SAzymes with an Fe-N-S-C asymmetric coordination structure. S doping induces distortion of the nitrogen coordination plane and disrupts charge distribution, affecting the electronic structure of the Fe active sites. Enzyme kinetics and DFT calculations show that S doping enhances both POD-like and GSHOx-like activities, promoting H_2O_2 decomposition and $^{\bullet}OH$ generation. The GSHOx-like activity depletes intracellular GSH, increasing oxidative stress and triggering ferroptosis. FNS SAzymes exhibit photothermal effects under laser irradiation, which can stimulate co-loaded AIPH to rapidly generate $^{\bullet}R$. The FNSA-MN, fabricated using vacuum-assisted centrifugation, demonstrates exceptional mechanical properties and rapid dissolution, along with controllable drug release kinetics. *In vitro* and *in vivo* experimental results reveal that FNSA-MN exhibits potent cytotoxicity against tumor cells, enhancing ferroptosis-based therapy with strong antitumor efficacy. Furthermore, FNSA-MN is capable of triggering an immune response within the body, effectively inhibiting tumor growth and metastasis. Our research proposes a novel coordination strategy to enhance ferroptosis and offers a promising platform for future tumor treatment and diagnostic approaches.

Declaration of competing interest

The authors declare that they have no known competing financial interests or personal relationships that could have appeared to influence the work reported in this paper.

CRediT authorship contribution statement

Jingyao Yu: Writing – original draft, Formal analysis, Data curation. **Zhuoran Yang:** Writing – original draft, Formal analysis, Data curation. **Jian Jiang:** Visualization, Data curation. **Mengshu Xu:** Formal analysis. **Chunyu Yang:** Writing – review & editing, Project administration, Funding acquisition. **Zhuo Li:** Writing – review & editing, Methodology. **Wei Guo:** Writing – review & editing, Funding acquisition, Conceptualization.

Acknowledgments

This work was supported by the National Natural Science Foundation of China (Nos. 52102344, 22105052), China Postdoctoral Science Foundation (No. 2021M701125).

Supplementary materials

Supplementary material associated with this article can be found, in the online version, at doi:10.1016/j.cclet.2025.111693.

References

[1] B.R. Stockwell, Cell 185 (2022) 2401–2421.
[2] S.J. Dixon, J.A. Olzmann, Nat. Rev. Mol. Cell Biol. 25 (2024) 424–442.
[3] J. Li, F. Cao, H. Yin, et al., Cell Death Dis. 11 (2020) 88.
[4] S.J. Dixon, K.M. Lemberg, M.R. Lamprecht, et al., Cell 149 (2012) 1060–1072.
[5] B.R. Stockwell, J.P.F. Angeli, H. Bayir, et al., Cell 171 (2017) 273–285.
[6] M. Wen, J. Ouyang, C. Wei, et al., Angew. Chem. Int. Ed. 58 (2019) 17425–17432.
[7] R.A. Gatenby, R.J. Gillies, J.S. Brown, Nat. Rev. Cancer 10 (2010) 526–527.
[8] X. Dai, Y. Zhu, M. Su, et al., Adv. Funct. Mater. 33 (2023) 2215022.
[9] Y. Lin, X. Chen, C. Yu, et al., Acta Biomater. 159 (2023) 300–311.
[10] H. Yang, X. Yao, Y. Liu, et al., ACS Nano 17 (2023) 15328–15353.
[11] D. Liang, A.M. Minikes, X. Jiang, Mol. Cell 82 (2022) 2215–2227.
[12] L. Gao, J. Zhuang, L. Nie, et al., Nat. Nanotechnol. 2 (2007) 577–583.
[13] N. Song, Y. Yu, Y. Zhang, et al., Adv. Mater. 36 (2024) 2210455.
[14] F. Zhu, J. He, L. Kong, et al., Nano Res. 18 (2025) 94907189.
[15] C. Ding, J. Min, Y. Tan, et al., Adv. Mater. 36 (2024) 2401361.
[16] W. You, Z. Cai, F. Xiao, et al., Adv. Sci. 12 (2025) 2417314.
[17] K. Wang, Y. Zhang, W. Mao, et al., Adv. Funct. Mater. 32 (2022) 2109221.
[18] T. Bai, P. Xue, S. Shao, et al., Adv. Sci. 11 (2024) 2405826.

[19] Y. Huang, J. Ren, X. Qu, Chem. Rev. 119 (2019) 4357–4412.
[20] M. Liang, X. Yan, Acc. Chem. Res. 52 (2019) 2190–2200.
[21] S. Ji, B. Jiang, H. Hao, et al., Nat. Catal. 4 (2021) 407.
[22] Z. Guo, J. Hong, N. Song, et al., Acc. Mater. Res. 5 (2024) 347–357.
[23] W. Lai, Z. Miao, Y. Wang, et al., Adv. Energy Mater. 9 (2019) 1900722.
[24] W. He, J. Wu, J. Liu, et al., Adv. Funct. Mater. 34 (2024) 2312116.
[25] L. Huang, J. Chen, L. Gan, et al., Sci. Adv. 5 (2019) eaav5490.
[26] C. Jin, S. Fan, Z. Zhuang, et al., Nano Res. 16 (2023) 1992–2002.
[27] P. Qi, J. Zhang, Z. Bao, et al., ACS Appl. Mater. Interfaces 14 (2022) 19081–19090.
[28] J. Pei, R. Zhao, X. Mu, et al., Biomater. Sci. 8 (2020) 6428–6441.
[29] B. Xu, S. Li, L. Zheng, et al., Adv. Mater. 34 (2022) 2107088.
[30] Y. Chen, P. Wang, H. Hao, et al., J. Am. Chem. Soc. 143 (2021) 18643–18651.
[31] Y. Chen, B. Jiang, H. Hao, et al., Angew. Chem. 135 (2023) e202301879.
[32] W. Liu, K. Wang, L. Gong, et al., Chem. Eng. J. 431 (2021) 134269.
[33] Y. Zhu, W. Wang, P. Gong, et al., ACS Nano 17 (2023) 3064–3076.
[34] W. Song, C. Xiao, J. Ding, et al., Adv. Mater. 36 (2023) 2301477.
[35] R. Niu, Y. Liu, B. Xu, et al., Adv. Mater. 36 (2024) 2312124.
[36] J. Liu, J. Zhu, H. Xu, et al., ACS Catal. 14 (2024) 6952–6964.
[37] Q. Lei, D. He, L. Ding, et al., Adv. Funct. Mater. 32 (2022) 2113269.
[38] T. Peng, Y. Chen, X. Luan, et al., Bioact. Mater. 45 (2025) 274–300.
[39] S. Gao, Y. Rao, X. Wang, et al., Adv. Mater. 36 (2024) 2307585.
[40] T. Hu, L. Jia, H. Li, et al., Adv. Healthc. Mater. 13 (2024) 2303147.
[41] S. Khan, A. Hasan, F. Attar, et al., J. Control. Release 338 (2021) 341–357.
[42] Z. Xiao, J. Yu, M. Feng, et al., J. Environ. Chem. Eng. 12 (2024) 113009.
[43] Y. Xiang, T. Liu, B. Jia, et al., Biosens. Bioelectron. 220 (2022) 114895.
[44] C. Sui, R. Tan, Y. Chen, et al., Bioconjug. Chem 32 (2021) 318–327.
[45] S. Chen, X. Li, C. Kao, et al., Angew. Chem. Int. Ed. 61 (2022) e202206233.
[46] S. Wei, M. Sun, J. Huang, et al., J. Am. Chem. Soc. 146 (2024) 33239–33248.
[47] X. Li, Y. Liu, F. Fu, et al., Nano-Micro Lett. 11 (2019) 68.
[48] W. Li, Z. Yang, C. Yang, et al., J. Colloid Interface Sci. 683 (2024) 132–146.
[49] F. Wu, Y. Du, J. Yang, et al., ACS Nano 16 (2022) 3647–3663.
[50] F. Shen, D. Tao, R. Peng, et al., Biomaterials 283 (2022) 121428.
[51] Q. Guo, X. Xu, X. Lai, et al., Exploration 5 (2025) 20230115.
[52] Y. Zhao, G. Zhu, X. Wang, et al., Chin. Chem. Lett. 37 (2026) 111031.
[53] Z. Yang, Z. Li, C. Yang, et al., Adv. Sci. 12 (2024) 2410621.
[54] H. Wu, G. Cao, M. Liu, et al., Chin. Chem. Lett. 36 (2025) 110493.
[55] H. Zhang, C. Liang, X. Ding, et al., Chin. Chem. Lett. 36 (2025) 110525.